PNAS RESEARCH ARTICLE | DEVELOPMENTAL BIOLOGY

A molecular timer couples organism-wide temporal identity to developmental checkpoints

Peipei Wu[a], Jing Wang[a], Brett Pryor[b], Isabella Valentino[b], David F. Ritter[c], Kaiser Loel[d], Olya Yarychkivska[e], Shai Shaham[e], Justin Kinney[d], Sevinc Ercan[c], Leemor Joshua-Tor[a,f], and Christopher M. Hammell[a,1]

Affiliations are included on p. 10.

Edited by Victor R. Ambros, University of Massachusetts Medical School, Worcester, MA; received February 25, 2026; accepted April 6, 2026

Coordinated development requires that growth and cell-fate transitions occur in a defined temporal order across tissues, yet how multicellular organisms generate and synchronize developmental timing information remains unclear. In *Caenorhabditis elegans*, stage-specific cell-fate transitions are driven by pulsatile transcription of microRNAs, including *lin-4* and *let-7* family members, but the mechanism that produces these rhythms has been unknown. Here, we identify a developmental timer composed of the transcription factor MYRF-1 and the PERIOD-like repressor LIN-42 that operates synchronously across all somatic tissues. MYRF-1 binds conserved regulatory elements upstream of heterochronic microRNA genes and drives once-per-stage transcriptional pulses that are phase-locked across tissues, while simultaneously activating *lin-42* expression. Newly synthesized LIN-42 directly associates with MYRF-1, limiting its nuclear residence and transcriptional activity and thereby constraining the amplitude and duration of each pulse. Beyond regulating stage-specific gene expression, we show that MYRF-1 activity is also required to license a developmental checkpoint essential for growth and successful ecdysis. Together, these findings define a reciprocal transcriptional–translational feedback loop that generates organism-wide developmental timing information, coupling tissue-specific differentiation programs to coordinated organismal growth through a shared molecular timer.

heterochronic | microRNA | temproal patterning | developmental Clock | checkpoint

Significance

Development requires that cells change identity in the correct order while the organism continues to grow. How multicellular animals generate and synchronize this timing information across tissues has remained unclear. We identify a molecular timer that coordinates developmental progression in the nematode *Caenorhabditis elegans* . A conserved transcription factor, MYRF-1, and the PERIOD-like protein LIN-42 form a feedback circuit that produces once-per-stage pulses of gene expression across the body. These pulses not only activate stage-specific regulatory RNAs but also gate passage through developmental checkpoints required for growth and molting. This work shows how rhythmic gene regulation can be converted into irreversible developmental transitions, revealing a mechanism by which an organism can measure developmental time and coordinate growth with differentiation.

During animal development, various cell types must acquire specialized identities while remaining coordinated with organismal growth. Such coordination depends not only on correct fate specification but also on the alignment of fate transitions across tissues, ensuring that proliferation, differentiation, and morphogenesis unfold in the proper relative sequence. Yet the mechanisms that generate this organism-wide temporal coherence remain unclear. It is unknown whether distinct cell lineages share a unified temporal program for measuring developmental time, or whether timing instead emerges from lineage-intrinsic regulatory architectures that independently encode the timing of fate transitions.

In *C. elegans*, the sequence of temporal patterning is controlled by a conserved heterochronic gene network, centered on key heterochronic microRNAs (miRNAs) that enforce synchronous, stage-specific cell-fate transitions across tissues (1–7). These miRNAs repress transcription factors and RNA-binding proteins that normally coordinate stage-specific proliferation, differentiation, and morphogenesis, and block the precocious onset of later developmental programs (8, 9). Mutations in heterochronic miRNAs disrupt the progression of temporal events throughout the organism, highlighting their global role in developmental transitions (1, 2, 5). Interestingly, heterochronic miRNAs are transcribed in sharp, once-per-larval-stage bursts in proliferating blast cells, differentiating epithelia, intestinal cells, glia, and postmitotic neurons (10–13). Although their rhythmic expression parallels the oscillatory transcription of many protein-coding genes, the two processes operate on distinct organizational scales: Oscillatory messenger RNAs display a wide range of tissue-specific expression windows within each larval stage (14, 15), whereas heterochronic miRNAs are transcribed in a shared phase of each larval stage across most somatic tissues (12, 16).

This synchrony raises a central question: Are heterochronic miRNAs regulated across somatic cells by lineage-specific transcriptional programs that require unique transcription factor networks to repeatedly converge on a common timing, or does a shared molecular mechanism enforce organism-wide coherence? Several cell-type-specific transcription factors modulate miRNA dynamics in individual tissues (13, 17), yet none have been shown to drive the global, once-per-stage transcriptional bursts necessary for system-wide coordination. In contrast, both genetic analyses and direct measurements of miRNA

Author contributions: P.W., J.W., B.P., I.V., D.F.R., L.J.-T., and C.M.H. designed research; P.W., J.W., B.P., I.V., D.F.R., S.E., L.J.-T., and C.M.H. performed research; O.Y. and S.S. contributed new reagents/analytic tools; K.L., J.K., and C.M.H. analyzed data; and P.W. and C.M.H. wrote the paper.

The authors declare no competing interest.

This article is a PNAS Direct Submission.

[1]To whom correspondence may be addressed. Email: chammell@cshl.edu.

This article contains supporting information online at https://www.pnas.org/lookup/suppl/doi:10.1073/pnas.2606846123/-/DCSupplemental.

Published May 6, 2026.

transcriptional dynamics in animals harboring mutations in *lin-42,* encoding the nematode ortholog of the circadian regulator *Period*, suggest that LIN-42 acts as a widespread transcriptional repressor of miRNA genes whose own expression is pulsatile and phase-coherent across somatic tissues (12, 13, 18–21). These properties indicate that LIN-42 acts as a key regulator of organism-wide timing and heterochronic miRNA transcription, even though *C. elegans* does not encode orthologs of the transcription factors that are usually repressed by Period in other systems (such as Clock and Bmal in mice and humans, or Clock and Cycle in *Drosophila*). Together, these observations highlight a central mechanistic gap: Although LIN-42 imposes soma-wide temporal coordination of heterochronic miRNA transcription, the upstream activator that generates these synchronized pulses and the logic by which this system aligns gene expression with developmental progression have remained undefined.

Here, we show that developmental timing is governed by interactions between LIN-42 and the conserved DNA-binding factor MYRF-1. Prior studies demonstrated that the *myrf-1* gene encodes an essential transcription factor that, like *lin-42*, generates rhythmic, once per larval stage protein expression in all somatic tissues (*SI Appendix*, Fig. S1) (10, 14, 15, 22, 23). Genetic analysis places *myrf-1* in early larval development and upstream of the transcriptional activation of the heterochronic miRNA *lin-4*: loss of *myrf-1* function strongly reduces activity of a *lin-4* transcriptional reporter and decreases mature *lin-4* RNA levels (23). Notably, the onset of MYRF-1 nuclear accumulation coincides with the initiation of *lin-4* transcription, suggesting direct transcriptional control (23) and precedes the transcription of *lin-42* at each larval stage (*SI Appendix*, Fig. S1). We demonstrate that MYRF-1 and LIN-42 physically interact to form a molecular timer that operates within a transcriptional/translational feedback circuit across somatic tissues. Temporal coherence is imposed by this unified circuit, which synchronizes miRNA transcription with developmental progression and converts transcriptional pulses into coordinated growth and irreversible cell-fate transitions.

Results

MYRF-1 Regulates the Expression of Heterochronic miRNAs and *lin-42*. To define the genomic targets of MYRF-1, we performed ChIP–seq on staged animals expressing an endogenously tagged GFP::MYRF-1 fusion at peak nuclear abundance during the L1 stage. This analysis identified ~1,000 high-confidence MYRF-1 binding sites, predominantly located within 3 kb of transcription start sites of potential MYRF-1 target genes (Fig. 1*A* and Dataset S1). Target genes were significantly enriched for regulators of temporal patterning, larval development, and ribosome biogenesis (*SI Appendix*, Fig. S2*a*). Strikingly, MYRF-1 binding was strongly enriched at conserved regulatory regions upstream of all heterochronic miRNA genes (Fig. 1*B*), as well as at promoters of key oscillatory regulators, including *lin-42* (Fig. 1*C*), and multiple genes required for molting (*nhr-23, grh-1*) (*SI Appendix*, Fig. S2 *C* and *D*). Motif analysis of sequences overrepresented in MYRF-1

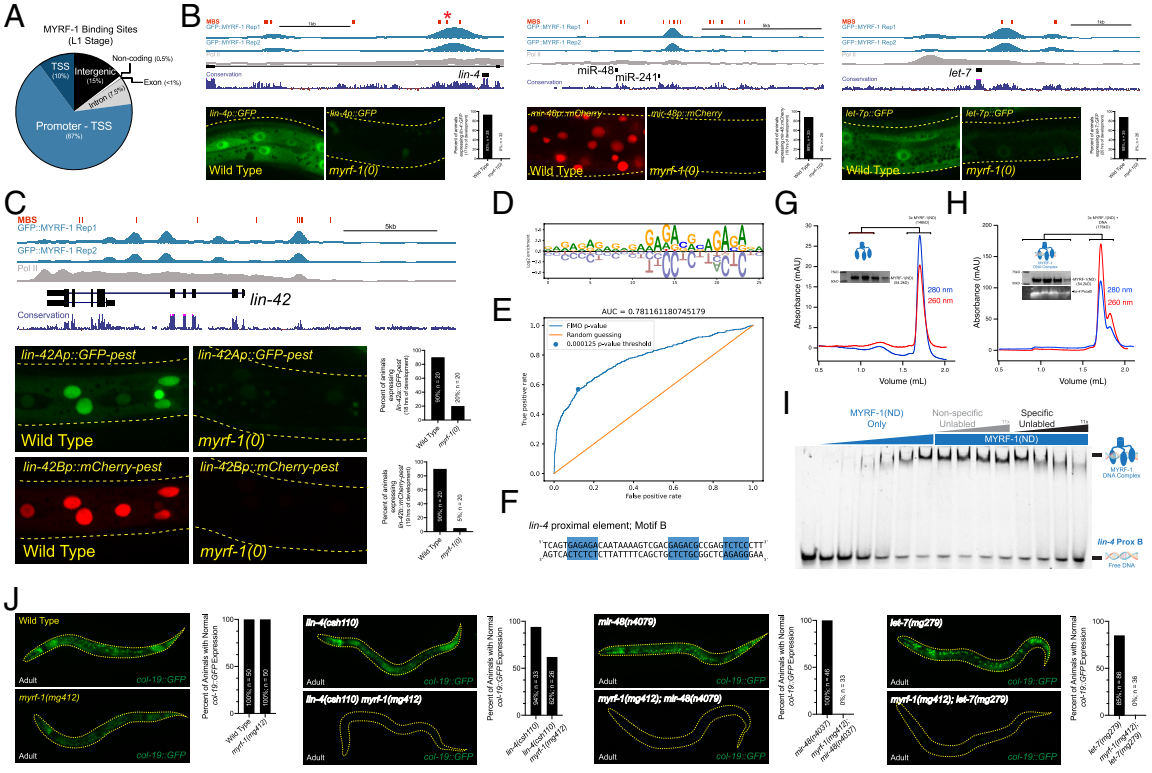

Fig. 1. MYRF-1 controls temporal patterning by binding regulatory sequences upstream of heterochronic microRNAs and *lin-42*. (*A*) Genome-wide distribution of MYRF-1–bound peaks identified by ChIP-seq. (*B* and *C*) MYRF-1 binding sites are enriched within putative regulatory regions of cyclically expressed heterochronic microRNAs and the *lin-42* gene. Transcriptional reporters for these MYRF-1 target loci require *myrf-1* for expression, indicating direct transcriptional activation. (*D*) Motif analysis of MYRF-1–bound sequences identifies a consensus motif characterized by a repetitive GA-rich core. (*E*) Receiver operating characteristic (ROC) curve evaluating the predictive power of the MYRF-1 binding motif. (*F*) Example of a consensus MYRF-1 binding site from the *lin-4* regulatory region (proximal element, Motif B), corresponding to the motif shown in panel *D*. The genomic location of this site is indicated by an asterisk in panel *A*. (*G* and *H*) Recombinant MYRF-1(ND) purifies as a homotrimer and binds the *lin-4* proximal element Motif B in vitro, as shown by size-exclusion chromatography and DNA-binding assays. MYRF-1 trimers also bind DNA fragments encompassing Motifs A and C within the *lin-4* proximal element (*SI Appendix*, Fig. S3 *A*–*C*). (*I*) Binding of trimeric MYRF-1 to *lin-4* proximal element Motif B is sequence-specific and is not competed by nonspecific competitor DNA. (*J*) A hypomorphic *myrf-1* allele (*myrf-1(mg412)*) does not disrupt expression of an adult-specific transcriptional reporter (*col-19p::GFP*) but strongly enhances temporal patterning defects caused by mutations in heterochronic miRNAs.

peaks revealed a conserved GA-rich sequence composed of three elements with defined orientation and spacing (Fig. 1 *D* and *E*), consistent with multimeric DNA binding. In agreement with this model, a recombinant MYRF-1 protein fragment (residues 1-483) that corresponds to the MYRF-1(ND) purifies as a trimeric complex (Fig. 1*G* and *SI Appendix*, Fig. S3*A*) and binds specifically to a 44-bp element within the proximal *lin-4* regulatory region (proxB) (Fig. 1*I*) that conforms to the MYRF-1 consensus motif (Fig. 1 *B*, *D*, and *F*). This MYRF-1:proxB binary complex forms stably in vitro and elutes at a volume consistent with a trimer on DNA according to size exclusion chromatography and mass photometry (Fig. 1*H* and *SI Appendix*, Fig. S3). Trimeric MYRF-1 also binds DNA corresponding to additional MYRF-1 consensus binding sites (Motif A and Motif C) in the *lin-4* proximal binding region (*SI Appendix*, Fig. S3 *B–E*).

To define the requirement for MYRF-1 in developmental gene activation, we analyzed transcriptional reporters in *myrf-1* null mutants that arrest during the L1 molt and early L2 stage (24). In wild-type larvae, heterochronic miRNA transcriptional reporters—including *lin-4* and *let-7* family members—and other cyclically expressed miRNAs—including *mir-1* were robustly expressed, whereas all were completely silent in *myrf-1(0)* animals (Fig. 1*B* and *SI Appendix*, Fig. S2*B*). In contrast, among oscillatory protein-coding targets examined, only *lin-42* expression depended on MYRF-1, while other molting regulators remained active (Fig. 1*C* and *SI Appendix*, Fig. S2 *C* and *D*). These results establish MYRF-1 as a direct transcriptional activator of heterochronic miRNAs and *lin-42* and reveal that rhythmic gene expression during larval development is generated by at least two mechanistically distinct regulatory systems.

We reasoned that if MYRF-1 controls heterochronic miRNA expression at larval stages after L1, then partial loss of MYRF-1 activity should enhance phenotypes associated with miRNA mutants that act during the L2-adult stages of development. This type of genetic interaction would lead to the reiteration of distinct cell-fate specification events at later larval stages. The *myrf-1(mg412)* allele alters amino acids near the predicted DNA-binding domain of MYRF-1, leading to an inappropriate reiteration of the larval molting cycle in adults (24). Importantly, *myrf-1(mg412)* mutant animals do not exhibit heterochronic phenotypes and properly express an adult-specific *col-19p::GFP* reporter (Fig. 1*J* and *SI Appendix*, Table S1) However, combining *myrf-1(mg412)* with a hypomorphic *lin-4* allele (*lin-4(csh110)*) produced synthetic phenotypes, including reduced *col-19p::GFP* expression in adult-stage animals and loss of alae structures on adult cuticles (Fig. 1*J*, Table 1, and *SI Appendix*, Table S1). *myrf-1(mg412)* also strongly enhanced defects in a *mir-48* deletion mutant, *mir-48(n4097)*, resulting in the failure of adult epidermal differentiation, reiteration of L2-stage

Table 1. *C. elegans myrf* genes genetically interact with multiple heterochronic mutants to control temporal patterning

	Percent of animals with Adult-specific alae formation*							
	L4 stage				Adult stage			
Genotype†	none	gapped	full	n =	none	gapped	full	n =
Wild type @20 °C	100	0	0	20	0	0	100	20
Wild type @15 °C	100	0	0	20	0	0	100	20
myrf-1(mg412) @20 °C	100	0	0	20	0	0	100	22
myrf-1(mg412) @15 °C	100	0	0	20	0	0	100	22
myrf-2(gk669)	100	0	0	20	0	0	100	20
myrf-1(mg412); myrf-2(gk669)	100	0	0	20	0	0	100	20
lin-42(n1089)	9	30	61	23	0	35	65	20
lin-42(n1089) myrf-1(mg412)	100	0	0	20	0	5	95	21
lin-42(n1089); myrf-2(gk669)	30	65	5	20	0	59	41	22
lin-42(n1089) myrf-1(mg412); myrf-2(gk669)	100	0	0	22	0	0	100	20
lin-42(ok2385)	29	38	33	24	0	33	67	21
lin-42(ok2385) myrf-1(mg412)	90	0	10	20	0	0	100	25
lin-46(ma164) @20 °C	–	–	–	–	0	0	100	21
lin-46(ma164) @15 °C	–	–	–	–	0	70	30	20
myrf-1(mg412); lin-46(ma164) @20 °C	–	–	–	–	0	0	100	20
myrf-1(mg412); lin-46(ma164) @15 °C	–	–	–	–	9	91	0	22
lin-4(e912)	–	–	–	–	100	0	0	21
lin-4(csh110)	–	–	–	–	4	50	46	24
lin-4(csh111)	–	–	–	–	0	29	71	21
lin-4(csh110 csh111)	–	–	–	–	90	10	0	21
myrf-1(mg412) lin-4(csh110)	–	–	–	–	61	26	13	23
mir-48(n4097)	–	–	–	–	0	0	100	20
myrf-1(mg412); mir-48(n4097)	–	–	–	–	77	23	0	22
let-7(mg279)	–	–	–	–	0	0	100	20
myrf-1(mg412); let-7(mg279)	–	–	–	–	42	58	0	24
lin-42(csh86 (ΔMBD1))	100	0	0	20	0	0	100	24
lin-42(csh83 (ΔMBD2))	100	0	0	21	0	0	100	20
lin-42(csh83 csh86 (ΔMBD1+2))	22	46	32	22	0	55	45	20

*Presence and quality (Gapped or Complete) of cuticular alae structures were assayed by Normarski DIC optics. Only one side of each animal was scored.
†Animals contain *maIs105*, which expresses an adult-specific, *col-19p::GFP* reporter integrated on chromosome V.

cell division programs during L3 stage, and defective production of adult-specific alae structures (Fig. 1*J*, Table 1, and *SI Appendix*, Fig. S4*A*).

Consistent with a broad role in temporal progression, even in late temporal cell fate transitions, *myrf-1(mg412)* enhanced defects in a *let-7* hypomorphic mutant (*let-7(mg279)*) (Fig. 1*J* and Table 1) and exhibited stage-specific synthetic phenotypes when combined with mutations in factors that prime heterochronic miRNA transcription (*blmp-1*) or modulate posttranslational repression of HBL-1 (*lin-46*) (*SI Appendix*, Fig. S4 *B–D*). Importantly, RNAi-mediated depletion of *hbl-1* fully suppressed these late-stage synthetic phenotypes, indicating that MYRF-1 promotes temporal progression primarily by enabling heterochronic miRNA–mediated repression of temporal identity genes (*SI Appendix*, Fig. S4*C*). Together, these results demonstrate that MYRF-1 acts broadly and cooperatively within the heterochronic pathway to ensure proper temporal progression, primarily by driving the transcription of heterochronic miRNAs.

Chromatin Accessibility Dictates MYRF-1 Functionality in Diverse Cell Lineages. To determine whether MYRF-1 binding upstream of *lin-4* is necessary for correct temporal patterning among diverse cell lineages, we integrated our ChIP-seq-defined MYRF-1 binding site data with cell-type–resolved chromatin accessibility maps derived from single-cell ATAC-seq experiments (25). Both MYRF-1 binding regions upstream of *lin-4* are within accessible chromatin in hypodermal lineages at the L2 stage (Fig. 2*A*). In contrast, only the proximal MYRF-1 binding region is accessible in neuronal lineages (Fig. 2*A*), indicating that MYRF-1-dependent regulation of *lin-4* may be limited by lineage-specific chromatin structure. The functional contribution of these elements was then probed genetically by using CRISPR/Cas-9 genome editing to delete either the distal or proximal MYRF-1 binding regions individually or in combination in the endogenous context (Fig. 2*A*). Deletion of either element alone produced minimal developmental defects and regular expression of temporal patterning reporters in hypodermal tissues (Fig. 2*B* and Table 1). By contrast, simultaneous deletion of both regions resulted in highly penetrant heterochronic phenotypes that closely phenocopied *lin-4(0)* mutant defects (Fig. 2*B*, Table 1, and *SI Appendix*, Table S1), demonstrating that MYRF-1 binding to either site is sufficient to support normal hypodermal temporal patterning and that both accessible enhancers bound by MYRF-1 are functionally redundant in developing nematode hypodermal cells.

Despite this redundancy in the hypodermis, deletion of the proximal element (*lin-4(csh110)*) caused a fully penetrant egg-laying defective phenotype (n = 120) that was absent in wild-type (n = 60) or in animals lacking the distal enhancer element, *lin-4(csh111)* (n = 100), revealing a lineage-specific requirement for MYRF-1 input. This defect correlated with failure of vulval precursor cell (VPC) maturation (Fig. 2*B* and *SI Appendix*, Table S2). Moreover, even in *csh110* animals with grossly normal VPC lineages, axons of the Hermaphrodite-Specific Neuron (HSN) that promote egg laying in adulthood failed to extend and innervate adult vulval structures and the ventral nerve chord, closely resembling the neuronal defects observed in *lin-4(0)* mutants (*SI Appendix*, Fig. S5) (26). These findings suggest that neuronal and vulval lineages are more sensitive to loss of the proximal MYRF-1 binding region than hypodermal tissues.

To directly examine the consequences of these cis-regulatory perturbations on *lin-4* function, we monitored the temporal expression dynamics of its direct target, the transcription factor LIN-14. In wild-type animals, *lin-4* expression during mid-L1 leads to repression of LIN-14 across somatic tissues (Fig. 2*C*) (2, 3, 27). As expected, *lin-4(0)* mutants fail to repress LIN-14, resulting in persistent LIN-14::GFP expression in both hypodermal and neuronal lineages (Fig. 2*C*) (28). In *lin-4(csh110)* animals, LIN-14::GFP was properly downregulated in hypodermal cells by the end of L1, but persisted at high levels in neurons, closely resembling the neuronal levels of LIN-14::GFP in adult *lin-4(0)* mutants (Fig. 2*C*). By contrast, LIN-14 regulation in *lin-4(csh111)* mutants was indistinguishable from wild type.

Consistent with these lineage-specific defects in LIN-14 regulation, *lin-4(csh110)* animals showed pronounced temporal mosaicism: Hypodermal cells executed normal temporal programs and matured to nearly normal adult hypodermis, whereas multiple neuronal cell types displayed fully penetrant juvenile phenotypes (Fig. 2 *D* and *E*). These phenotypes include alterations in neuropeptide expression patterns (e.g., NLP-45::T2A::GFP::H2B) that are directly regulated by LIN-14 and *lin-4* expression (28), as well as the perdurance of L1-stage expression programs [e.g., *oig-1* expression (29)] in later larval stages that antagonize the stage-specific rewiring of motor neuron synapses in the ventral nerve chord. Together, these results show that MYRF-1 binding sites upstream of *lin-4* are required across somatic lineages, and lineage-specific differences in miRNA transcriptional regulation reflect chromatin accessibility patterns rather than distinct timing mechanisms. Thus, organism-wide temporal coherence of heterochronic miRNA expression arises from global coordination of MYRF-1 acting on shared cis-regulatory elements, rather than from repeated convergence of tissue-restricted transcriptional programs.

LIN-42 Physically Binds to MYRF-1. Gene regulatory networks that generate pulsatile transcriptional patterns typically rely on coupled negative feedback and delay mechanisms in which transcription factors activate their own repressors, producing periodic bursts of gene expression with defined phase, amplitude, and duration (30). Because MYRF-1 directly activates *lin-42* (Fig. 1*C*) and LIN-42 is predicted to dampen transcriptional pulses (12, 13), we asked whether LIN-42 physically associates with MYRF-1. Yeast two-hybrid (Y2H) assays showed that both major LIN-42 isoforms (LIN-42A and LIN-42B) robustly interact with the NDs of MYRF-1 and MYRF-2 (Fig. 3*A*), suggesting that these interactions may be part of a transcription/translational feedback loop (TTFL) mechanism. A hallmark feature of TTFL circuits is reciprocal buffering, in which an asymmetry in regulatory interactions caused by a loss-of-function mutation in one component can be suppressed by a loss-of-function mutation in the other (31). We therefore tested whether *myrf1/2(lf)* and *lin-42(lf)* mutations modulate each other's developmental timing phenotypes. The hypomorphic allele *myrf-1(mg412)* induces a supernumerary adult molting phenotype marked by aberrant *mlt-10p::GFP-pest* reactivation in adult animals (24). Combining a *lin-42(lf)* allele with *myrf-1(mg412)* fully suppressed these defects (Fig. 3 *B* and *C*). Conversely, the precocious heterochronic phenotypes associated with multiple *lin-42(lf)* alleles were eliminated when combined with *myrf-1(mg412)* (Fig. 3 *D* and *E*, Table 1, and *SI Appendix*, Table S1). *myrf-2(0)* mutations, which alone do not elicit detectable molting or temporal patterning phenotypes, also partially suppress precocious adult-alae formation observed in *lin-42(lf)* animals (Table 1). These reciprocal genetic interactions indicate that MYRF-1 and LIN-42 mutually regulate each other's activity in vivo and support their placement in a shared feedback loop.

To define the molecular basis of this interaction, we used AlphaFold 3 (32) to model complexes of MYRF-1(ND) and LIN-42. The predicted structures revealed two distinct LIN-42B

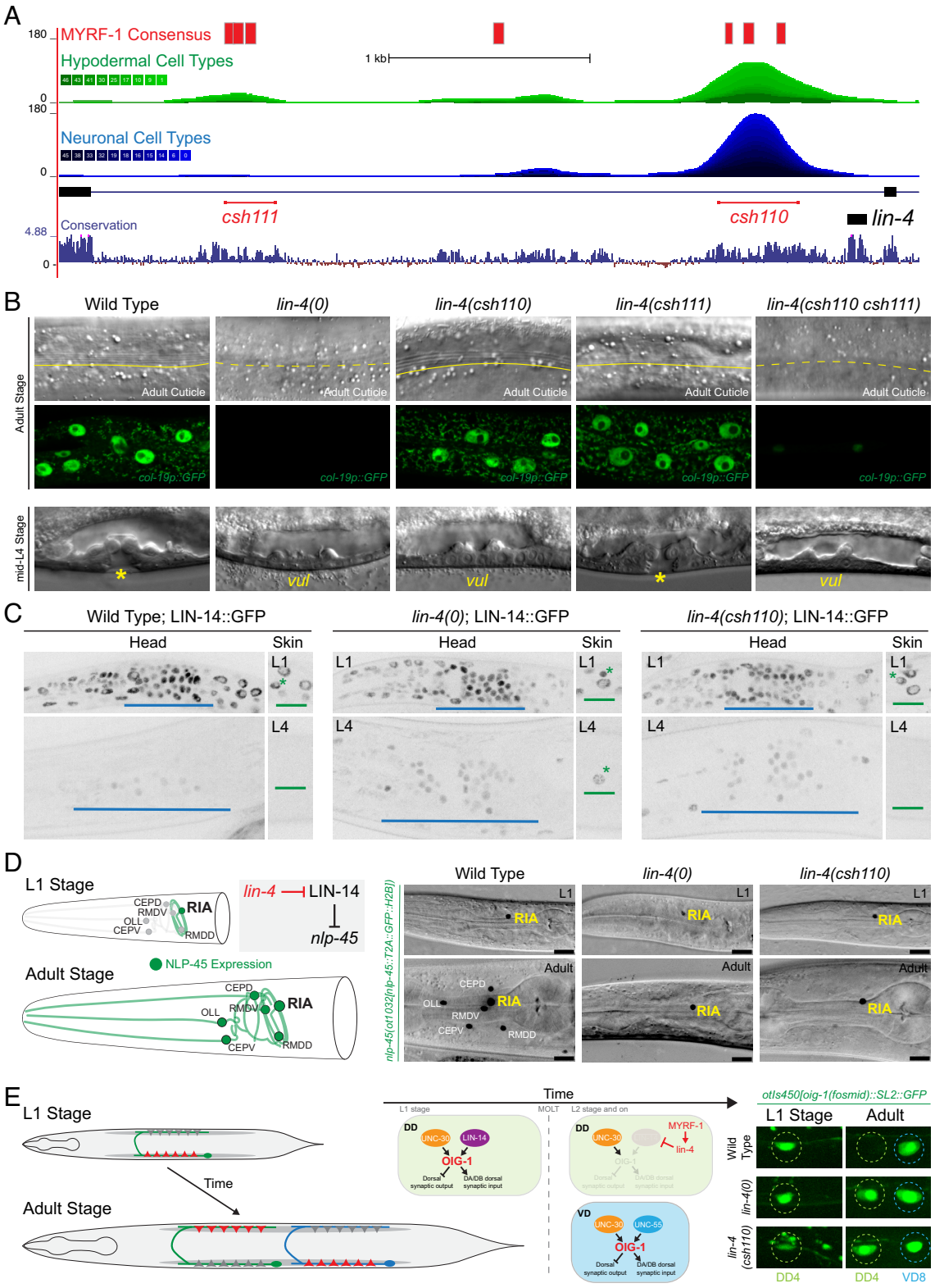

Fig. 2. Tissue-specific requirements for MYRF-1 binding sites at the *lin-4* locus. (*A*) Schematic of the *lin-4* locus showing GFP::MYRF-1 ChIP-seq binding sites (gray) and predicted MYRF-1 consensus motifs (red). Genome browser tracks display chromatin accessibility in hypodermal (green) and neuronal (blue) cell types from L2-stage single-cell ATAC-seq. Conservation across nematode species is shown below, together with the positions of the *lin-4(csh111)* and *lin-4(csh110)* alleles, which delete distinct clusters of MYRF-1 binding sites. (*B*) Representative micrographs of adult cuticle morphology and *col-19p::GFP* expression, and of L4-stage vulval development, in animals of the indicated genotypes. (*C*) Dynamics of LIN-14::GFP expression in wild-type and *lin-4* mutant animals. Blue bars indicate LIN-14::GFP expression in head neuronal ganglia, and green bars indicate expression in hypodermal tissues; green asterisks mark lateral seam cells expressing LIN-14::GFP at the indicated stages. (*D*) Schematic and representative images of *nlp-45* expression in head ganglion neurons. Following LIN-14 downregulation at the end of L1, *nlp-45* expression normally expands to additional sensory and motor neurons; this expansion fails in *lin-4(0)* and *lin-4(csh110)* mutants. Images show *nlp-45::T2A::GFP::H2B* reporter expression in staged animals of the indicated genotypes. Phenotypes are fully penetrant in late L4 (0% wild type, n = 25; 100% *lin-4(0)*, n = 25; 100% *lin-4(csh110)*, n = 22). (*E*) Persistent expression of an *oig-1p::GFP* transcriptional reporter in DD neurons of *lin-4* mutants. In both *lin-4(0)* and *lin-4(csh110)* animals, reporter expression persists into late L4, whereas it is fully extinguished in wild type (0/25 wild type; 20/20 *lin-4(0)*; 22/23 *lin-4(csh110)*).

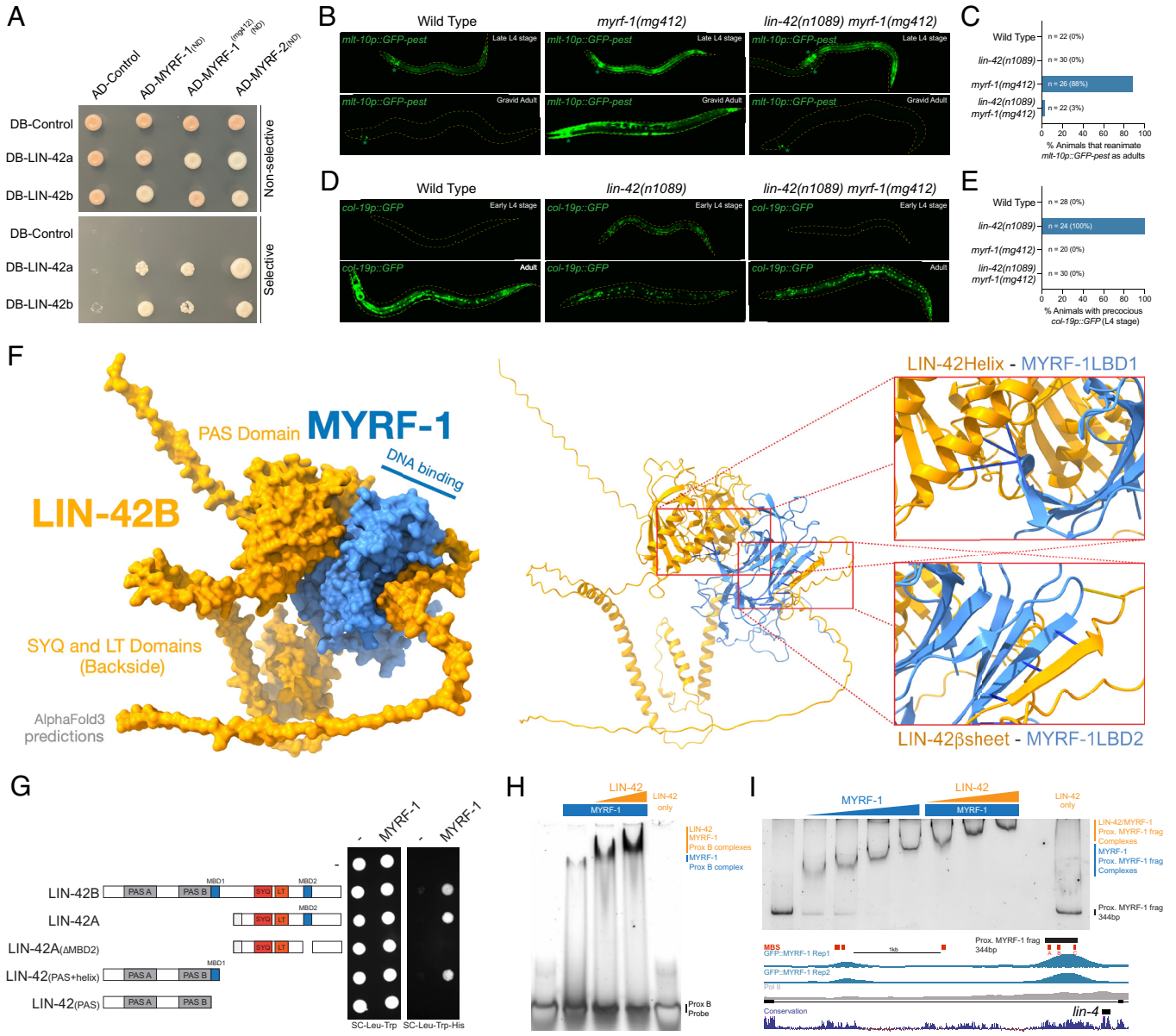

Fig. 3. LIN-42 and MYRF-1 interact physically, genetically, and functionally. (*A*) Yeast two-hybrid assays show that both LIN-42 isoforms physically associate with the N-terminal nuclear fragment of *C. elegans* MYRF proteins. Both LIN-42 isoforms also interact with the hypomorphic MYRF-1 variant MYRF-1(mg412). (*B* and *C*) The hypomorphic allele *myrf-1(mg412)* causes a highly penetrant supernumerary molting phenotype and reactivation of an adult *mlt-10p::GFP-PEST* transcriptional reporter. Loss of *lin-42* suppresses both phenotypes when combined with *myrf-1(mg412)*, indicating a strong genetic interaction. (*D* and *E*) Conversely, precocious expression of the adult-specific *col-19p::GFP* transcriptional reporter in *lin-42(lf)* mutants is suppressed by concomitant loss of *myrf-1*, demonstrating reciprocal genetic dependence between the two factors in temporal patterning. (*F*) AlphaFold3 structural predictions indicate that LIN-42 engages two distinct interaction surfaces on a MYRF-1 monomer. MYRF-1-binding domain 1 (MBD1) corresponds to a conserved α-helical region immediately C-terminal to the LIN-42 PAS domains, whereas MYRF-1-binding domain 2 (MBD2) comprises a β-strand that extends an existing β-sheet in the predicted MYRF-1 structure. (*G*) Two-hybrid assays using LIN-42 truncation constructs lacking residues predicted to form MBD1 or MBD2 show that both regions are required for efficient LIN-42–MYRF-1 interaction. (*H*) Addition of recombinant LIN-42B into electrophoretic mobility shift assays containing MYRF-1(ND) and the *lin-4* proximal element Motif B indicates that LIN-42 can supershift MYRF-1/DNA complexes. Recombinant LIN-42B does not bind the *lin-4* proximal element Motif B by itself. (*I*) Electrophoretic mobility shift assays demonstrate that increasing concentrations of recombinant MYRF-1 bind a *lin-4* proximal regulatory element upstream of *lin-4* in a stepwise manner, consistent with sequential occupancy of three predicted MYRF-1 trimer-binding sites (Prox A, B, and C). This element corresponds to the region deleted in the *lin-4(csh110)* allele (Fig. 2*A*). Addition of recombinant LIN-42B alone does not bind DNA, indicating that LIN-42 associates specifically with DNA-bound MYRF-1 complexes.

domains that bind separate sites of MYRF-1(ND) (Fig. 3*F*). The first interface is mediated by a conserved α-helical extension immediately C-terminal to the LIN-42B PAS domain (MBD1), whereas the second involves a LIN-42B β-strand segment (MBD2) that intercalates into a β-fold domain of MYRF-1. To test these predictions, we generated LIN-42 deletion constructs lacking either the PAS-adjacent α-helix or the β-strand–forming segment and retested Y2H interactions between these proteins. Deletion of either segment from LIN-42 fragments abolished MYRF-1–LIN-42 association in yeast, whereas constructs retaining either motif preserved robust binding (Fig. 3*G*). These results support features of the structural predictions for this complex and indicate that specific LIN-42 domains are required for interaction with MYRF-1.

We next tested whether LIN-42 influences MYRF-1 DNA binding using electrophoretic mobility shift assays (EMSAs) with the motif B-DNA fragment from the *lin-4* proximal element. Addition of recombinant LIN-42B to reactions containing DNA-bound MYRF-1 produced supershifted complexes (Fig. 3*H*), whereas

LIN-42B alone did not bind this fragment, indicating that the supershifts result from direct interactions with MYRF-1. Reactions with the *lin-4* proximal element motif A and C were similar (*SI Appendix*, Fig. S6). We extended this analysis to the longer *lin-4* proximal fragment deleted in the *csh110* allele, which contains three predicted MYRF-1 consensus sites (Fig. 3*I*). Titration of MYRF-1 yielded three discrete protein–DNA complexes, consistent with sequential occupancy of these sites by MYRF-1 homotrimers. Addition of LIN-42B generated a corresponding stepwise series of supershifted complexes, again without detectable DNA binding by LIN-42B alone (Fig. 3*H*). EMSAs using each binding element in isolation showed that a single MYRF-1 trimer binds each site and is independently supershifted by LIN-42B, supporting the conclusion that the multistep supershifts observed with the full-length fragment reflect additive LIN-42 association with DNA-bound MYRF-1 complexes (*SI Appendix*, Fig. S6).

LIN-42 Posttranslationally Controls the Duration of MYRF-1 Expression. To assess the functional importance of the LIN-42/MYRF-1 interaction domains in vivo, we used CRISPR/Cas9 editing to delete the two LIN-42 domains suspected to mediate direct MYRF-1 binding: the PAS-adjacent α-helical region (*lin-42(csh86))* and the predicted, C-terminal β-strand segment *(lin-42(csh83)*). Animals lacking these individual domains showed normal larval cell division patterns, expressed *col-19p::GFP* only in adulthood, and developed adult alae at the correct time (Table 1 and *SI Appendix*, Table S1). Strikingly, simultaneous deletion of both domains, *lin-42(csh83 csh86)*, caused strong precocious phenotypes characteristic of significant *lin-42* loss of function, including early *col-19p::GFP* expression in L4-stage animals and the premature formation of adult-specific alae after the L3 molt (Fig. 4*A*, Table 1, and *SI Appendix*, Table S1) (13, 18). These findings demonstrate that the two LIN-42 structural motifs function together in vivo and that most LIN-42 functions required for temporal cell-fate specification depend on its ability to interact with MYRF-1.

Given the dynamic, once-per-larval-stage expression pattern of *myrf-1* (*SI Appendix*, Fig. S1*A*) and LIN-42's role in repressing the transcription of MYRF-1 targets (12, 13, 20, 33), we hypothesized that LIN-42 might posttranslationally regulate MYRF-1 dynamics. To test this, we tracked GFP::MYRF-1 expression in L4-staged hypodermal cells, where GFP::MYRF-1 levels could be directly correlated with specific developmental milestones (13, 34). GFP::MYRF-1 was first observed on the outer membranes of lateral seam cells in early L4 animals (L4.0 stage) (Fig. 4*B*). Soon after initial detection in the membrane, cleaved GFP::MYRF-1(ND) started transitioning to the nucleus and was fully nuclear by the L4.3 stage (Fig. 4*B* and *SI Appendix*, Fig. S7*A*). GFP::MYRF-1 levels then decreased starting at L4.4 and were absent from lateral seam cell nuclei by the L4.6 stage. These dynamic expression patterns were also seen in other somatic cells (*SI Appendix*, Fig. S7*B*). We examined GFP::MYRF-1 in animals with a large *lin-42* deletion allele, *lin-42(n1089),* or animals expressing the LIN-42 variant (LIN-42(csh83 csh86)) that cannot bind MYRF-1. In both *lin-42* mutant strains, early L4 GFP::MYRF-1 expression dynamics (membrane localization followed by nuclear import) remained unchanged (Fig. 4*B* and *SI Appendix*, Fig. S7*A*). However, nuclear MYRF-1 expression dynamics are significantly altered in *lin-42* loss-of-function mutants, with nuclear MYRF-1 expression persisting in somatic cells for up to 1.5-2 extra hours (Fig. 4*C* and *SI Appendix*, Fig. S7 *A* and *B*) (34). The prolonged nuclear accumulation of MYRF-1 in *lin-42* mutants coincides with an extended period of *lin-4* transcriptional activity in *lin-42* mutants (13), indicating that the timing of MYRF-1 nuclear activity determines the length, and likely the amplitude of *lin-4* transcriptional output.

Acute Depletion of MYRF-1 Results in Developmental Arrest at the End of Each Molt. As noted above, null alleles of *myrf-1* cause fully penetrant larval arrest, with animals failing to shed the L1 cuticle at the end of the L1 molt and remaining in a developmentally quiescent state for several days before death (22, 24). Using an auxin-inducible degradation system to acutely deplete AID*::GFP::MYRF-1 during postembryonic development (Fig. 4*C*), we found that loss of MYRF-1 can trigger a stable developmental arrest at any larval stage, in which animals fail to complete the molting cycle and terminally arrest within an unshed cuticle (Fig. 4*D*). These arrests persist for several days, indicating that MYRF-1 depletion induces a durable, nontransient block to development. Arrested animals exhibit coordinated defects at multiple levels: cell divisions cease (including seam cell divisions), morphogenetic programs such as vulval and gonadal development halt, and overall somatic growth stops. Arrest outcomes are bimodal and depend on developmental timing: Depletion of MYRF-1 prior to the stage-specific MYRF-1 pulse causes arrest at the subsequent molt, whereas depletion after this pulse permits completion of the current and next stage but results in arrest at the following molt. Notably, depletion during the peak of nuclear MYRF-1 expression yields both outcomes within the same cohort, revealing a narrow, stage-specific permissive window (Fig. 4*D*). Together, these findings identify a MYRF-1–dependent, stage-coupled developmental checkpoint whose passage requires timely MYRF-1 activity.

Discussion

This work identifies MYRF-1 as a central regulator of postembryonic development that serves two coupled functions: It drives stage-specific temporal programming through heterochronic miRNAs and licenses passage through a developmental checkpoint required for successful ecdysis, growth, and progression to the next larval stage (Fig. 4*E*). Through reciprocal regulation with the PERIOD-like repressor LIN-42, MYRF-1 forms a transcriptional–translational feedback loop that functions as a molecular timer, generating once-per-stage oscillations in gene expression. In this circuit, MYRF-1 activates transcription of *lin-42* and heterochronic miRNAs, while LIN-42 feeds back to constrain the duration of each MYRF-1 pulse, thereby controlling the phase, amplitude, and duration of miRNA transcription. We hypothesize that LIN-42 likely accelerates the normal degradation of MYRF-1 by facilitating interactions with the normal turnover machinery. Prior experiments indicate that MYRF-1 physically interacts with multiple components of the ubiquitin ligase complex, and LIN-42 may facilitate these interactions to modulate MYRF-1 turnover rate (35).

The synchronization of these pulses across somatic tissues and their alignment with developmental transitions indicate that this timer coordinates temporal gene expression at the organismal level. Importantly, the stage-specific and bimodal arrest phenotypes revealed by acute MYRF-1 depletion demonstrate that this timing circuit is directly coupled to a developmental checkpoint that governs whether growth and differentiation can proceed. MYRF-1 target genes that enable bypassing each larval checkpoint are likely genetically separable from those implicated in scheduling stage-specific developmental gene regulatory programs, as mutations in heterochronic miRNA genes do not elicit developmental arrest phenotypes (1, 5, 7, 36). Importantly, multiple MYRF-1

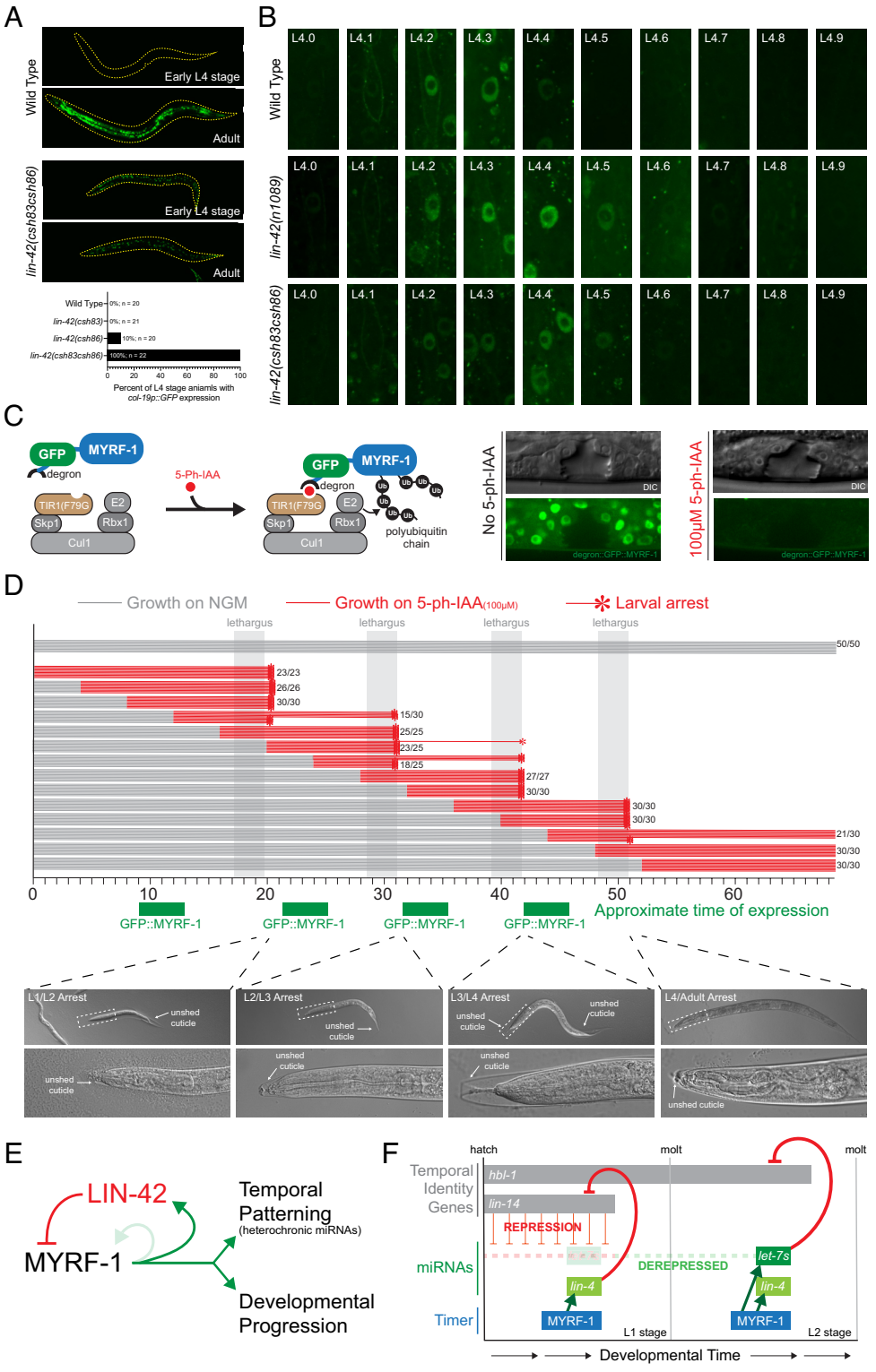

Fig. 4. MYRF-1 activity is regulated by LIN-42 and is required for continuous postembryonic development. (*A*) Deletion of both MYRF-1–binding regions in LIN-42 results in strong heterochronic phenotypes, including precocious expression of an adult-specific transcriptional reporter. (*B*) Model of MYRF-1 maturation and nuclear entry. MYRF-1 is synthesized in the cytoplasm, inserted into the endoplasmic reticulum, trafficked to the membrane, and autocatalytically cleaved to release an N-terminal fragment that translocates to the nucleus and activates target gene transcription. In *lin-42(n1089)* mutants and in *lin-42* alleles lacking both MYRF-1–binding domains [*lin-42(csh83 csh86)*], MYRF-1 nuclear residency is prolonged. (*C*) Schematic of the auxin-inducible degron system (AIDv2) used for acute depletion of degron::GFP::MYRF-1 via TIR1(F79G)–dependent recruitment to the endogenous SCF ubiquitin ligase following addition of 5-Ph-IAA. (*D*) Time-resolved depletion of MYRF-1 reveals stage-specific requirements for larval progression. (*Top*) Synchronized larvae were initiated at L1 and transferred at defined times to 5-Ph-IAA to induce acute MYRF-1 depletion. Depletion during discrete temporal windows caused arrest at the subsequent larval molt, whereas depletion outside these windows allowed completion of that molt but resulted in arrest after the following molt. (*Bottom*) Representative terminal phenotypes, including arrest during ecdysis within an unshed cuticle and persistent seam cell identity marked by failure of seam cell fusion and continued reporter expression after 2 d. (*E*) Model of genetic and regulatory interactions between *myrf-1* and *lin-42*. MYRF-1 activates transcription of *lin-42*, which in turn limits MYRF-1 activity, shaping the temporal output of the circuit. Downstream targets include heterochronic microRNAs that specify temporal identity and additional effectors required for developmental progression at each larval molt. (*F*) Model illustrating how stage-restricted MYRF-1 activity generates pulsatile transcription of heterochronic microRNAs, leading to the sequential downregulation of temporal identity genes across larval development.

targeted genes exhibit larval arrest phenotypes like *myrf-1(0)* mutants (37, 38). Therefore, MYRF-1 not only schedules developmental gene regulatory programs but also links temporal patterning to the physiological execution of repeated developmental transitions (Fig. 4*E*).

A critical feature of the developmental timer is that its activity within each larval stage is embedded in the nested-repression architecture of the heterochronic pathway (9, 39, 40). Each stage is defined by temporal identity genes that both activate the stage-appropriate transcriptional program and repress the miRNAs expressed in the subsequent stage (8, 41). As the temporal identity gene declines late in the stage, repression of the corresponding miRNA loci is relieved, but transcription does not occur immediately (Fig. 4*F*). We hypothesize that derepression licenses transcriptional competence, whereas activation is imposed by the subsequent MYRF-1 pulse, which arrives only after the next cell fate has been specified (Fig. 4*F*). This delay ensures that miRNA expression follows, rather than precedes, fate commitment, and the resulting miRNA expression wave in the subsequent stage represses the next temporal identity gene, converting rhythmic MYRF-1/LIN-42 activity into irreversible developmental transitions.

Although the MYRF-1/LIN-42 circuit shares transcriptional–translational feedback logic with circadian oscillators (30, 42), its function is fundamentally different. Rather than preparing tissues for recurrent environmental cycles, this timer schedules a finite series of sequential developmental events that must occur once and in order. By coupling rhythmic transcription to checkpoint control and nested repression, the circuit transforms pulsatile gene expression into coordinated organismal growth. These findings suggest that conserved clock components can be repurposed to measure developmental time and synchronize differentiation across tissues, revealing a general principle by which multicellular systems align gene regulatory dynamics with irreversible biological transitions.

Materials and Methods

***C. elegans* Strains and Maintenance.** *C. elegans* strains were maintained on standard nematode growth medium (NGM) plates seeded with *Escherichia coli* OP50 at 20 °C or 15 °C under standard laboratory conditions (43). The Bristol N2 isolate was used as the wild-type reference strain. A complete list of strains used in this study is provided in *SI Appendix*, Table S3.

CRISPR Genome Deletion and GFP Tagging. Genome editing and endogenous GFP tagging were performed by following established CRISPR/Cas9 protocols (44, 45). Briefly, Cas9–sgRNA ribonucleoprotein (RNP) complexes were preassembled by combining purified recombinant Cas9 protein with synthetic CRISPR sgRNAs targeting specific genomic loci, together with a *dpy-10* sgRNA used as a co-CRISPR marker to generate Roller phenotypes. The injection mixture, containing the assembled RNP complexes and a PCR-amplified repair template with flanking homology arms, was injected into the germline of hermaphrodites. Broods segregating Roller progeny were screened for genome edits, and putative transgenic animals were subsequently genotyped by PCR and sequenced to confirm domain deletions within the *lin-42* gene, MYRF-1 binding sequences upstream of *lin-4*, or endogenous GFP tagging at the *myrf-1* N terminus. All oligos, sgRNAs, and repair templates can be found in *SI Appendix*, Table S4.

Yeast Two-Hybrid Assays. Plasmids encoding target proteins fused to GAL4 DNA-binding-domain (pBD) and GAL4 Activation Domain (pAD) were cotransformed into the pJ69-4a Y2H yeast strain (46) using the lithium acetate method as previously described in the Matchmaker™ GAL4 Two-Hybrid System 3 User Manual (Takara Bio USA, Inc.). Transformants were selected on SC-TRP-LEU plates for 3 d at 30 °C. Three independent colonies from each transformation were subsequently spotted onto SC–HIS–TRP–LEU plates. Protein–protein interactions were inferred from visible growth on 3-AT conditions with negative growth in empty vector controls after 3 d of incubation at 30 °C. Plasmids used in two-hybrid assays can be found in *SI Appendix*, Table S5.

ChIP-seq. Endogenously GFP-tagged MYRF-1 animals were synchronized at the L1 stage by hypochlorite treatment of gravid adults followed by overnight hatching in M9 buffer. Synchronized L1 larvae were plated on 150-mm NGM plates seeded with *E. coli* OP50 and grown for ~11 h, when GFP::MYRF-1 is predominantly localized to the nucleus. Approximately 100 μL of packed worms were collected by washing in M9 buffer, crosslinked in 2% formaldehyde, and quenched with 125 mM glycine. Two biological replicates were collected for each ChIP experiment. ChIP–seq was performed as previously described (13). Briefly, crosslinked animals were homogenized in FA buffer (50 mM HEPES–KOH pH 7.5, 150 mM NaCl, 1 mM EDTA, 1% Triton X-100, 0.1% sodium deoxycholate, and 0.1% sarkosyl) supplemented with protease inhibitors, dounce-homogenized on ice, and sonicated at 4 °C to shear DNA and generate 200 to 800 bp chromatin fragments. Clarified extracts were quantified by Bradford assays, and 1 to 4 mg of total protein was incubated overnight at 4 °C with anti-GFP antibody (Abcam, #ab290) and anti-RNA polymerase II antibody (Millipore 05-952-I-). Immune complexes were captured with protein A/G Sepharose beads, sequentially washed with buffers of increasing stringency, and eluted in SDS-containing ChIP elution buffer. Crosslinks were reversed overnight at 65 °C, followed by RNase A and Proteinase K treatments. DNA was purified using Qiagen MinElute columns and analyzed for fragment size before library preparation and sequencing with Illumina NextSeq500 at NYU Center for Genomics and Systems Biology core facility.

ChIP-Seq Data Analysis and MYRF-1 Binding Motif Identification. Single-end 75 bp ChIP and input control reads were processed using established computational pipelines. Raw sequences were first assessed for quality with FastQC and FastQ Screen, and low-quality reads were removed using Trimmomatic. Adapter sequences were trimmed with Cutadapt, and the filtered reads were aligned to the *C. elegans* reference genome (ce11) using Bowtie2 (47). MACS2 (48, 49) was used for peak calling, with input DNA as the control, and significance thresholds of $P < 0.001$ and $q < 0.05$ were applied. Reproducible peaks across biological replicates were identified by intersecting using BedTools (50). A random set of genomic regions matched in number and length to the reproducible peaks was generated as background controls. Peak and control sequences were analyzed with the MEME suite in discriminative mode using a first-order (dinucleotide) background model. Two enriched motifs were identified: a predominant GA-repeat motif (dimeric or trimeric) present in most peaks, and a less repetitive secondary motif found in a smaller subset. These motifs were scanned across the peak and control sequences using FIMO (51), and the resulting *P*-values of the top hits were used to generate ROC curves. The GA-repeat motif achieved an area under the curve (AUC) of 0.78, and the secondary motif, 0.73. Based on these curves, motif significance thresholds were set at $P < 1 \times 10^{-4}$ and $P < 1 \times 10^{-3}$ for the GA-repeat and secondary motifs, respectively. Genome-wide motif scanning was then performed using these thresholds, and the resulting motif distributions were visualized as custom UCSC Genome Browser tracks. GO enrichment analysis was performed using WormEnrichr (52, 53). Biological Process GO terms were ranked by the Enrichr combined score ($c = \log(p) \times z$), where *p* reflects statistical significance and *z* indicates the strength of enrichment relative to random expectation.

Confocal Imaging. For confocal imaging, worms at the appropriate developmental stages were mounted on 2% (w/v) agarose pads in 100 mM levamisole (Sigma). Images were acquired using a Hamamatsu Orca EM-CCD camera and a Borealis-modified Yokagawa CSU-10 spinning disk confocal microscope (Nobska Imaging, Inc.) with a Plan-APOCHROMAT x 100/1.4, 63×/1.3, or 40/1.4 oil DIC objective controlled by Visiview Software (version: 7.0). LED illumination at 488 nm and 561 nm was used to excite green and red fluorophores, respectively. Images were processed in ImageJ (Fiji) using identical processing settings for all genotypes and developmental stages within each experiment.

Quantification of Fluorescent Reporter. The average intensity (arbitrary units) of GFP::MYRF-1 in hypodermal cells of L4-stage animals was quantified using ImageJ as previously described (13, 17). For each cell, fluorescence intensity was calculated as the nuclear signal minus the background signal measured from the same image. The mean intensity of three hypodermal cells was used to

determine the GFP::MYRF-1 level for each animal. All statistical analyses were performed using GraphPad Prism 9 (GraphPad Software, San Diego, Ca). Mean ± SEM values were calculated and plotted in Prism. Differences between the two groups were considered statistically significant when $P < 0.05$ (Student's *t* test).

Recombinant Protein Expression and Purification. *C. elegans* MYRF-1(ND) (amino acids 1-483) and full-length LIN-42B were cloned as N-terminal Strep-SUMO fusion proteins in separate pFL vectors of the MultiBac Baculovirus expression system (54). These proteins were individually expressed in Sf9 cells grown in CCM3 media (Hy-Clone) at 27 °C for 60 h. Cells were pelleted by centrifugation at 1,800 rpm for 20 min, resuspended in lysis buffer (MYRF-1 = 25 mM Tris pH 8, 200 mM NaCl, 2 mM DTT, 10% glycerol; LIN-42B = 20 mM Tris pH 8, 200 mM NaCl, 5 mM BME) and sonicated in the presence of homemade protease inhibitor cocktail and cOmplete mini EDTA-free protease inhibitors (Roche). Lysates were clarified by ultracentrifugation (38 k for MYRF-1, 39 k for LIN-42B) for 1 h at 4 °C. For affinity chromatography, lysate supernatants were batch-bound to Strep-Tactin Superflow resin (IBA) for 1 h at 4 °C with rotation. Affinity beads were harvested by centrifugation at 1,000 rpm for 3 min, decanted to 1 column volume (CV), resuspended, and applied to a gravity column. For MYRF-1, the column was washed with 1 CV lysis buffer, 2 CV high salt wash buffer (25 mM Tris pH 8, 500 mM NaCl, 2 mM DTT, 10% glycerol), and 1 CV lysis buffer to remove nucleic acid and protein contaminants. For LIN-42B, the column was washed with 3 CV lysis buffer. Proteins were eluted with 5 mM desthiobiotin in lysis buffer. The strep-SUMO tag was removed from MYRF-1 by TEV protease (1:30 by mass) overnight at 4 °C. Proteins were further purified using anion-exchange (HiTrap Q at pH 8) and size-exclusion chromatography (Superose 6 increase, 10/300) in storage buffer (25 mM Tris pH 8, 200 mM NaCl, 2 mM DTT, 10% glycerol). Peak fractions were assessed for purity by SDS-PAGE, pooled, and concentrated to 0.6 mg/mL (MYRF-1) or 0.9 mg/mL (LIN-42B). To reconstitute the MYRF-1 trimer on DNA, fully purified MYRF-1 was incubated in a 5-molar excess with annealed prox A, B, or C DNA in MYRF-1 storage buffer on ice for 1 h. The DNA-bound trimer was separated by analytical gel filtration on a Superose 6 increase 3.2/300 in MYRF-1 storage buffer. Peak fractions were analyzed by SDS-PAGE and gels were stained with SYBR gold (1:33 k in ddH2O) at room temperature (RT) for 10 min to highlight copurified DNA.

Electrophoretic Mobility Shift Assays. For competition assays, 1.18 μM MYRF-1 was incubated with 70 nM ATTO 680-labeled proxB on ice for 5 min, after which competitor oligos were added. Reactions were incubated for an additional 15 min at RT and run on 5% TBE gels in 0.5× TBE at 135 V for 35 min at 4 °C. MYRF-1 titration experiments with unlabeled proxA (50 nM) or proxC (65 nM) include up to an 8× molar excess of MYRF-1, and these reactions were incubated in the same manner as was done with proxB. For LIN-42B titration experiments, MYRF-1 was incubated with 55 nM unlabeled prox A, B, or C or 448 pM *lin-4* proximal promoter fragment in the presence of strep-SUMO-LIN-42B for 15 min at RT. Assays with prox A, B, or C used 221 nM MYRF-1 and include up to a 2× molar excess of LIN-42B (relative to MYRF), while those with the *-1lin-4* proximal promoter fragment used 720 nM MYRF-1 and include up to 6× molar excess LIN-42B. Reactions with LIN-42B and proxA, B, and C DNAs were run on 5% TBE gels in 0.5× TBE (pH adjusted to 9.0) at 110 V for 40 min, while those with the *lin-4* proximal promoter were run at 100 V for 90 min (TBE not pH adjusted after buffer preparation). All reactions were conducted in conditions similar to those used for the yeast homolog, Ndt80 (10 mM Tris pH 8, 75 mM KCl, 11 mM $MgCl_2$, 50 μm ZnSO4, 10% glycerol, 1 mM DTT, and 0.02% Tween-20), and all gels were prerun at 100 V for 30 min at 4 °C (55). Gels from experiments using ATTO 680 probe were imaged on the Typhoon FLA 7000 imager with the Cy5 channel, while those using unlabeled probes were stained with a 1:100 k dilution of SYBR gold in ice-cold 0.5× TBE for 3 min and destained for 5 min prior to imaging on a Bio-Radad ChemiDoc. A full list of the DNA reagents used in EMSAs can be found in *SI Appendix*, Table S6.

Mass Photometry. Recombinant MYRF-1(ND) was diluted to 1.2 μM and analyzed at 1/10 the prepared concentration in 1× PBS on untreated MassGlass UC slides (Reyfeyn). Movies were recorded in AcquireMP, and data were analyzed in DiscoverMP software (Reyfeyn). Beta-amylase derived from sweet potato was used to create the standard curve (Sigma-Aldrich).

Data, Materials, and Software Availability. Raw sequence reads for ChIP-seq data (56) and key *C. elegans* strains have been deposited in the Sequence Read Archive (SRA) and the Caenorhabditis Genetics Center (CGC), respectively. Other data are included in the article and/or the supporting information.

ACKNOWLEDGMENTS. We would like to thank Rad Utama, whose work is funded by the CSHL Cancer Center Support Grant (CCSG) (P30 CA045508). We thank the *Caenorhabditis* Genetics Center (CGC), which is funded by NIH Office of Research Infrastructure Programs (P40 OD010440), for the construction of several *let-7*-family miRNA transcriptional reporter strains. This work was supported by NIH grant R01GM155806 (C.M.H.); NIH grant R01GM117406 (C.M.H.); NIH grant R01GM155806 (L.J.-T.); NIH grant R35GM130311 (S.E.); National Human Genome Research Institute grant R01HG011787 (J.K.); National Institute of Health grant K99GM151467 (O.Y.); National Institute of Health grant R35NS105094 (S.S.); National Institute of Health grant R01HD103610 (S.S.); and NSF grant 2217560 (C.M.H.).

Author affiliations: [a]Cold Spring Harbor Laboratory, Cold Spring Harbor, NY 11724; [b]Cold Spring Harbor Laboratory School of Biological Sciences, Cold Spring Harbor, NY 11724; [c]Department of Biology, New York University, New York, NY 10003; [d]Simons Center for Quantitative Biology, Cold Spring Harbor Laboratory, Cold Spring Harbor, NY 11724; [e]Laboratory of Developmental Genetics, The Rockefeller University, New York, NY 10065; and [f]HHMI, W. M. Keck Structural Biology Laboratory, Cold Spring Harbor Laboratory, Cold Spring Harbor, NY 11724

1. V. Ambros, H. R. Horvitz, Heterochronic mutants of the nematode *Caenorhabditis elegans*. *Science* **226**, 409–416 (1984).
2. R. C. Lee, R. L. Feinbaum, V. Ambros, The *C. elegans* heterochronic gene lin-4 encodes small RNAs with antisense complementarity to lin-14. *Cell* **75**, 843–854 (1993).
3. B. Wightman, I. Ha, G. Ruvkun, Posttranscriptional regulation of the heterochronic gene *lin-14* by *lin-4* mediates temporal pattern formation in *C. elegans*. *Cell* **75**, 855–862 (1993).
4. F. J. Slack *et al.*, The *lin-41* RBCC gene acts in the *C. elegans* heterochronic pathway between the *let-7* regulatory RNA and the LIN-29 transcription factor. *Mol. Cell* **5**, 659–669 (2000).
5. B. J. Reinhart *et al.*, The 21-nucleotide let-7 RNA regulates developmental timing in *Caenorhabditis elegans*. *Nature* **403**, 901–906 (2000).
6. M. Li, M. W. Jones-Rhoades, N. C. Lau, D. P. Bartel, A. E. Rougvie, Regulatory mutations of mir-48, a *C. elegans* let-7 family microrna, cause developmental timing defects. *Dev. Cell* **9**, 415–422 (2005).
7. A. L. Abbott *et al.*, The let-7 microrna family members *mir-48*, *mir-84*, and *mir-241* function together to regulate developmental timing in *Caenorhabditis elegans*. *Dev. Cell* **9**, 403–414 (2005).
8. M. Ivanova, E. G. Moss, A temporal sequence of heterochronic gene activities promotes stage-specific developmental events in *Caenorhabditis elegans*. *G3 (Bethesda)* **14**, jkae130 (2024).
9. V. Ambros, A hierarchy of regulatory genes controls a larva-to-adult developmental switch in *C. elegans*. *Cell* **57**, 49–57 (1989).
10. D. h. Kim, D. Grün, A. van Oudenaarden, Dampening of expression oscillations by synchronous regulation of a microRNA and its target. *Nat. Genet.* **45**, 1337–1344 (2013).
11. P. M. Van Wynsberghe *et al.*, LIN-28 co-transcriptionally binds primary let-7 to regulate miRNA maturation in *Caenorhabditis elegans*. *Nat. Struct. Mol. Biol.* **18**, 302–308 (2011).
12. R. Perales, D. M. King, C. Aguirre-Chen, C. M. Hammell, LIN-42, the *Caenorhabditis elegans* PERIOD homolog, negatively regulates microRNA transcription. *PLoS Genet.* **10**, e1004486 (2014).
13. B. Kinney *et al.*, A circadian-like gene network programs the timing and dosage of heterochronic miRNA transcription during *C. elegans* development. *Dev. Cell* **58**, 2563–2579.e8 (2023).
14. G.-J. Hendriks, D. Gaidatzis, F. Aeschimann, H. Großhans, Extensive oscillatory gene expression during *C. elegans* larval development. *Mol. Cell* **53**, 380–392 (2014).
15. M. W. Meeuse *et al.*, Developmental function and state transitions of a gene expression oscillator in *Caenorhabditis elegans*. *Mol. Syst. Biol.* **16**, e9498 (2020).
16. S. Nahar *et al.*, Dynamics of miRNA accumulation during *C. elegans* larval development. *Nucleic Acids Res.* **52**, 5336–5355 (2024).
17. N. Stec *et al.*, An epigenetic priming mechanism mediated by nutrient sensing regulates transcriptional output during *C. elegans* development. *Curr. Biol.* **31**, 809–826.e6 (2021).
18. M. Jeon, H. F. Gardner, E. A. Miller, J. Deshler, A. E. Rougvie, Similarity of the *C. elegans* developmental timing protein LIN-42 to circadian rhythm proteins. *Science* **286**, 1141–1146 (1999).
19. J. M. Tennessen, H. F. Gardner, M. L. Volk, A. E. Rougvie, Novel heterochronic functions of the *Caenorhabditis elegans* period-related protein LIN-42. *Dev. Biol.* **289**, 30–43 (2006).
20. K. A. McCulloch, A. E. Rougvie, Caenorhabditis elegans period homolog lin-42 regulates the timing of heterochronic miRNA expression. *Proc. Natl. Acad. Sci. U.S.A.* **111**, 15450–15455 (2014).
21. P. M. Van Wynsberghe, A. E. Pasquinelli, Period homolog LIN-42 regulates miRNA transcription to impact developmental timing. *Worm* **3**, e974453 (2014).
22. J. Meng *et al.*, Myrf ER-bound transcription factors drive C. elegans synaptic plasticity via cleavage-dependent nuclear translocation. *Dev. Cell* **41**, 180–194.e7 (2017).
23. Z. Xu, Z. Wang, L. Wang, Y. B. Qi, Essential function of transmembrane transcription factor MYRF in promoting transcription of miRNA lin-4 during *C. elegans* development. *Elife* **12**, RP89903 (2024).
24. S. Russel, A. R. Frand, G. Ruvkun, Regulation of the *C. elegans* molt by pqn-47. *Dev. Biol.* **360**, 297–309 (2011).
25. T. J. Durham *et al.*, Comprehensive characterization of tissue-specific chromatin accessibility in L2 *Caenorhabditis elegans* nematodes. *Genome Res.* **31**, 1952–1969 (2021).

26. K. Olsson-Carter, F. J. Slack, A developmental timing switch promotes axon outgrowth independent of known guidance receptors. *PLoS Genet.* **6**, e1001054 (2010).
27. P. Arasu, B. Wightman, G. Ruvkun, Temporal regulation of *lin-14* by the antagonistic action of two other heterochronic genes, *lin-4* and *lin-28*. *Genes Dev.* **5**, 1825–1833 (1991).
28. H. Sun, O. Hobert, Temporal transitions in the post-mitotic nervous system of *Caenorhabditis elegans*. *Nature* **600**, 93–99 (2021).
29. K. Howell, J. G. White, O. Hobert, Spatiotemporal control of a novel synaptic organizer molecule. *Nature* **523**, 83–87 (2015).
30. J. M. Hurley, J. J. Loros, J. C. Dunlap, Circadian oscillators: Around the transcription-translation feedback loop and on to output. *Trends Biochem. Sci.* **41**, 834–846 (2016).
31. S. Becker-Weimann, J. Wolf, H. Herzel, A. Kramer, Modeling feedback loops of the mammalian circadian oscillator. *Biophys. J.* **87**, 3023–3034 (2004).
32. J. Abramson *et al.*, Accurate structure prediction of biomolecular interactions with AlphaFold 3. *Nature* **630**, 493–500 (2024).
33. P. M. Van Wynsberghe *et al.*, The period protein homolog LIN-42 negatively regulates microRNA biogenesis in *C. elegans*. *Dev. Biol.* **390**, 126–135 (2014).
34. D. Z. L. Mok, P. W. Sternberg, T. Inoue, Morphologically defined sub-stages of *C. elegans* vulval development in the fourth larval stage. *BMC Dev. Biol.* **15**, 26 (2015).
35. S. L. Xia *et al.*, The LRR-TM protein PAN-1 interacts with MYRF to promote its nuclear translocation in synaptic remodeling. *Elife* **10**, e67628 (2021).
36. M. Chalfie, H. R. Horvitz, J. E. Sulston, Mutations that lead to reiterations in the cell lineages of *C. elegans*. *Cell* **24**, 59–69 (1981).
37. H. M. Dalton, S. P. Curran, Hypodermal responses to protein synthesis inhibition induce systemic developmental arrest and AMPK-dependent survival in *Caenorhabditis elegans*. *PLoS Genet.* **14**, e1007520 (2018).
38. A. Surya, Q. Zhao, B. Voigt, R. Rangan, E. S. Cenik, Ribosomal biogenesis defects trigger subunit specific developmental checkpoints via TOR signaling and gap junction in *C. elegans*. *Dev. Biol.* **529**, 46–55 (2026).
39. E. G. Moss, Heterochronic genes and the nature of developmental time. *Curr. Biol.* **17**, R425–R434 (2007).
40. V. Ambros, Control of developmental timing in *Caenorhabditis elegans*. *Curr. Opin. Genet. Dev.* **10**, 428–433 (2000).
41. J. Tsialikas, M. A. Romens, A. Abbott, E. G. Moss, Stage-specific timing of the microRNA regulation of *lin-28* by the heterochronic gene *lin-14* in Caenorhabditis elegans. *Genetics* **205**, 251–262 (2017).
42. J. C. Dunlap, Molecular bases for circadian clocks. *Cell* **96**, 271–290 (1999).
43. S. Brenner, The genetics of *Caenorhabditis elegans*. *Genetics* **77**, 71–94 (1974).
44. A. Paix, A. Folkmann, D. Rasoloson, G. Seydoux, High efficiency, homology-directed genome editing in *Caenorhabditis elegans* using CRISPR-Cas9 ribonucleoprotein complexes. *Genetics* **201**, 47–54 (2015).
45. A. Paix, A. Folkmann, G. Seydoux, Precision genome editing using CRISPR-Cas9 and linear repair templates in C. elegans. *Methods* **121–122**, 86–93 (2017).
46. P. James, J. Halladay, E. A. Craig, Genomic libraries and a host strain designed for highly efficient two-hybrid selection in yeast. *Genetics* **144**, 1425–1436 (1996).
47. B. Langmead, C. Trapnell, M. Pop, S. L. Salzberg, Ultrafast and memory-efficient alignment of short DNA sequences to the human genome. *Genome Biol.* **10**, R25 (2009).
48. Y. Zhang *et al.*, Model-based analysis of ChIP-Seq (MACS). *Genome Biol.* **9**, R137–R139 (2008).
49. T. Liu, Use model-based analysis of ChIP-seq (MACS) to analyze short reads generated by sequencing protein-DNA interactions in embryonic stem cells. *Methods Mol. Biol.* **1150**, 81–95 (2014).
50. A. R. Quinlan, I. M. Hall, BEDTools: A flexible suite of utilities for comparing genomic features. *Bioinformatics* **26**, 841–842 (2010).
51. C. E. Grant, T. L. Bailey, W. S. Noble, FIMO: Scanning for occurrences of a given motif. *Bioinformatics* **27**, 1017–1018 (2011).
52. M. V. Kuleshov *et al.*, Enrichr: A comprehensive gene set enrichment analysis web server 2016 update. *Nucleic Acids Res.* **44**, W90–W97 (2016).
53. E. Y. Chen *et al.*, Enrichr: Interactive and collaborative HTML5 gene list enrichment analysis tool. *BMC Bioinformatics* **14**, 128 (2013).
54. S. Trowitzsch, C. Bieniossek, Y. Nie, F. Garzoni, I. Berger, New baculovirus expression tools for recombinant protein complex production. *J. Struct. Biol.* **172**, 45–54 (2010).
55. S. Chu, I. Herskowitz, Gametogenesis in yeast is regulated by a transcriptional cascade dependent on Ndt80. *Mol. Cell* **1**, 685–696 (1998).
56. P. Wu, D. Ritter, S. Ercan, C. Hammell, Data from "Genomic targets of C. elegans MYRF-1." Sequence Read Archive (SRA). https://www.ncbi.nlm.nih.gov/bioproject/PRJNA1419822. Deposited 6 February 2026.